

# Northumbria Research Link

Citation: Sun, Mengxuan, Li, Zhijie, Li, Hao, Wu, Zhonglin, Shen, Wenzhong and Fu, Richard (2020) Mesoporous Zr-doped CeO<sub>2</sub> nanostructures as superior supercapacitor electrode with significantly enhanced specific capacity and excellent cycling stability. *Electrochimica Acta*, 331. p. 135366. ISSN 0013-4686

Published by: Elsevier

URL: <https://doi.org/10.1016/j.electacta.2019.135366>  
<<https://doi.org/10.1016/j.electacta.2019.135366>>

This version was downloaded from Northumbria Research Link:  
<http://nrl.northumbria.ac.uk/id/eprint/41601/>

Northumbria University has developed Northumbria Research Link (NRL) to enable users to access the University's research output. Copyright © and moral rights for items on NRL are retained by the individual author(s) and/or other copyright owners. Single copies of full items can be reproduced, displayed or performed, and given to third parties in any format or medium for personal research or study, educational, or not-for-profit purposes without prior permission or charge, provided the authors, title and full bibliographic details are given, as well as a hyperlink and/or URL to the original metadata page. The content must not be changed in any way. Full items must not be sold commercially in any format or medium without formal permission of the copyright holder. The full policy is available online: <http://nrl.northumbria.ac.uk/policies.html>

This document may differ from the final, published version of the research and has been made available online in accordance with publisher policies. To read and/or cite from the published version of the research, please visit the publisher's website (a subscription may be required.)

# Mesoporous Zr-doped CeO<sub>2</sub> nanostructures as superior supercapacitor electrode with significantly enhanced specific capacity and excellent cycling stability

Mengxuan Sun<sup>1</sup>, Zhijie Li<sup>1\*</sup>, Hao Li<sup>1</sup>, Zhonglin Wu<sup>1</sup>, Wenzhong Shen<sup>2</sup>, YongQing

Fu<sup>3\*\*</sup>

<sup>1</sup>School of Physics, University of Electronic Science and Technology of China,  
Chengdu, 610054, P. R. China

<sup>2</sup>State Key Laboratory of Coal Conversion, Institute of Coal Chemistry, Chinese  
Academy of Science, Taiyuan, 030001, China

<sup>3</sup>Faculty of Engineering and Environment, Northumbria University, Newcastle Upon  
Tyne, NE1 8ST, UK

Zhijie Li (**Corresponding Author**): ORCID: 0000-0001-9870-9939;

\*E-mail: [zhijieli@uestc.edu.cn](mailto:zhijieli@uestc.edu.cn); TEL: +86 02883202160

Yong Qing Fu (**Corresponding Author**): ORCID: 0000-0001-9797-4036;

\*E-mail: [Richard.fu@northumbria.ac.uk](mailto:Richard.fu@northumbria.ac.uk); TEL: +44 (0)191 2274662

## **Abstract**

Due to its good chemical stability and outstanding redox properties, CeO<sub>2</sub> has been regarded as a promising electrode material for supercapacitors, but its specific capacity is quite low which restricts its wide-range applications. To enhance its specific capacity, in this study, specially designed mesoporous Zr-doped CeO<sub>2</sub> nanostructures with large surface area, extraordinarily high porosity and abundant oxygen vacancies were fabricated using a hydrothermal method and an assisted calcination process. The synthesized mesoporous CeO<sub>2</sub>-Zr-1 nanostructures (with an atomic ratio of Ce:Zr = 10:1) were composed of nanocrystals with an average size of 6.7 nm, and had a large surface area of 81.0 m<sup>2</sup> g<sup>-1</sup>, and abundant mesopores with a volume of 0.2108 cm<sup>3</sup> g<sup>-1</sup>. In 2 M KOH electrolyte, the CeO<sub>2</sub>-Zr-1 electrode generated a much larger specific capacity (448.1 C g<sup>-1</sup>) than that of the pristine CeO<sub>2</sub> (249.3 C g<sup>-1</sup>) at a current density of 1 A g<sup>-1</sup>. An asymmetric supercapacitor of CeO<sub>2</sub>-Zr-1//activated carbon produced a high energy storage density of 23.3 Wh kg<sup>-1</sup> at 398.5 W kg<sup>-1</sup>, and an excellent long-term cycling stability with 96.4% capacity retention after 6000 cycles.

**Key words:** CeO<sub>2</sub>, Hydrothermal, Mesoporous, Supercapacitor, Capacity

## 1. Introduction

Because of rapid depletion of fossil fuels and severe environmental pollution, clean and highly-efficient energy storage devices are greatly demanded. Supercapacitor, as one of the most promising clean and renewable energy storage techniques, has advantages such as high power density, short charging time, high rate capacity and good cycling stability [1-4]. In recent years, many metal oxide nanomaterials have been explored as the supercapacitor electrode materials [5], including RuO<sub>2</sub> [6], Co<sub>3</sub>O<sub>4</sub> [7, 8], NiO [9, 10], MnO<sub>2</sub> [11, 12], CuO [13], SnO<sub>2</sub> [14, 15], V<sub>2</sub>O<sub>5</sub> [16], Fe<sub>3</sub>O<sub>4</sub> [17, 18],  $\alpha$ -Fe<sub>2</sub>O<sub>3</sub> [19], TiO<sub>2</sub> [20] and CeO<sub>2</sub> [21, 22]. Among them, CeO<sub>2</sub> is an eco-friendly electrode material with low toxicity and excellent chemical stability, and can be operated in various acidic and alkaline electrolytes [23-26]. Furthermore, the fast transition between Ce(III) and Ce(IV) oxidation states makes the CeO<sub>2</sub> a promising electrode material for supercapacitors [27].

Accordingly, various CeO<sub>2</sub> nanostructures have been prepared to improve their electrochemical performance, such as nanospheres [21], nanorods [22, 28, 29], nanowires [21], nanoparticles [27, 30] and porous nanostructures [31], etc. However, at present the specific capacity produced from these CeO<sub>2</sub> nanostructures reported in literature are still quite low. For examples, CeO<sub>2</sub> nanorods exhibited a specific capacitance of 162.47 F g<sup>-1</sup> at the current density of 1 A g<sup>-1</sup> in the 3 M KOH electrolyte [22]. The CeO<sub>2</sub> nanospheres showed a specific capacitance of 142.5 F g<sup>-1</sup> at the current density of 0.25 A g<sup>-1</sup> in the Na<sub>2</sub>SO<sub>4</sub> electrolyte [27]. The porous CeO<sub>2</sub> exhibited a specific capacitance of 134.6 F g<sup>-1</sup> at the current density of 1 A g<sup>-1</sup> in the 1 M KOH

electrolyte [31].

In order to enhance its capacity, the CeO<sub>2</sub> has been modified using carbon nanomaterials. For examples, Deng et al [32] reported that composite of CeO<sub>2</sub> nanoparticles/multi-wall carbon nanotubes showed an enhanced large specific capacitance of 455.7 F g<sup>-1</sup> at the current density of 2 A g<sup>-1</sup> in the 1 M KOH electrolyte, while the specific capacitance of pristine CeO<sub>2</sub> nanoparticles was only 73.7 F g<sup>-1</sup>. Padmanathan et al [29] reported that the carbon coated CeO<sub>2</sub> nanorods achieved a large specific capacitance of 644 F g<sup>-1</sup> at a current density of 0.5 A g<sup>-1</sup> in the 3 M KOH electrolyte. Another method to enhance the specific capacitance of CeO<sub>2</sub> is doping with metal ions. For example, Murugan et al [26] prepared Co doped CeO<sub>2</sub> nanoparticles using a microwave synthesis method, and showed a much larger specific capacitance of 573 F g<sup>-1</sup> than that of pure CeO<sub>2</sub> nanoparticles (235 F g<sup>-1</sup>) at a current density of 2 A g<sup>-1</sup> in the 1 M KOH electrolyte. The specific capacitance of Ni doped CeO<sub>2</sub> nanoparticles was also reported to increase to 577 F g<sup>-1</sup> from the 235 F g<sup>-1</sup> of pure CeO<sub>2</sub> nanoparticles at the current density of 2 A g<sup>-1</sup> in the 1 M KOH electrolyte [30]. Although the specific capacities of these modified CeO<sub>2</sub> based electrode materials have been remarkably improved, these values are still not good enough for the practical applications [33, 34]. Therefore, it is still a great challenge to further optimize the CeO<sub>2</sub> nanostructures for achieving high specific capacity.

It is well known that the large surface area, abundant pores and hierarchical nanostructures are beneficial to their good electrochemical performance of electrode materials [35, 36]. Therefore, in order to obtain good electrochemical performance, it

is believed that design and fabrication of CeO<sub>2</sub> hierarchical nano-architectures with small nanocrystal size, large surface area and extraordinary porosity should be the best solution. Because Zr<sup>4+</sup> the same valence state and similar ionic radii with Ce<sup>4+</sup> ions, some Ce<sup>4+</sup> ions can be substituted by Zr<sup>4+</sup> ions in the CeO<sub>2</sub> in the synthesis process, which is facilitates to obtain the CeO<sub>2</sub> with small nanocrystal size, large surface area and extraordinary porosity [37]. Accordingly, in this study, we designed and fabricated mesoporous Zr-doped CeO<sub>2</sub> nanostructures using a hydrothermal method and an assisted calcination process in order to achieve high supercapacitor performance. The mesoporous Zr-doped CeO<sub>2</sub> nanostructures achieved extraordinary porosity, small nanocrystal size and large surface area. The extraordinary porosity and hierarchical nano-architecture can shorten the diffusion paths of the electrolyte and facilitate the efficient utilization of the active materials for enhancing the faradaic reactions. The small nanocrystals size and large surface area provide abundant active sites for the Faradaic redox reactions.

Our results using this specially designed electrode material showed that the mesoporous CeO<sub>2</sub>-Zr-1 nanostructure (with atomic ratio of Ce:Zr=10:1) exhibited a significantly enhanced specific capacity of 448.1 C g<sup>-1</sup> at a current density of 1 A g<sup>-1</sup>. An asymmetric supercapacitor (ASC) based on CeO<sub>2</sub>-Zr-1//activated carbon (AC) was further made and showed an energy storage density of 23.3 Wh kg<sup>-1</sup> at 398.5 W kg<sup>-1</sup>, and a good long-term cycling stability with only 3.6% capacity loss after 6000 cycles.

## **2. Experimental Section**

### **2.1 Synthesis and characterization of mesoporous Zr-doped CeO<sub>2</sub> nanostructures**

Mesoporous Zr-doped CeO<sub>2</sub> nanostructures with different Zr concentrations were synthesized using a hydrothermal method and an assisted calcination process. Firstly, 1 mmol ZrO(NO<sub>3</sub>)<sub>2</sub>·2H<sub>2</sub>O, 10 mmol Ce(NO<sub>3</sub>)<sub>3</sub>·6H<sub>2</sub>O and 5 mmol NaNO<sub>3</sub> were dissolved in 80 mL deionized water. Secondly, 20 mL of ammonia water (27 wt%) and 2 mL of hydrogen peroxide were successively added drop-by-drop into the above solution under a continuous stirring to form a reddish-brown sol. Thirdly, this sol was transferred into a Teflon-lined stainless autoclave (with a volume of 120 mL) for the hydrothermal reaction at 100 °C for 20 hrs. After the hydrothermal process, the precipitates were collected by filtering and washing using deionized water, and then dried at 60 °C for 10 hrs. Finally, the above precipitates were calcined at 500 °C in air for 4 hrs to obtain mesoporous Zr-doped CeO<sub>2</sub> nanostructure sample with an atomic ratio of Ce:Zr = 10:1 (named as sample of CeO<sub>2</sub>-Zr-1). Similarly, by changing the addition amounts of ZrO(NO<sub>3</sub>)<sub>2</sub>·2H<sub>2</sub>O in the above preparation processes (e.g., 0, 0.5 and 1.5 mmol), samples of the pristine CeO<sub>2</sub>, CeO<sub>2</sub>-Zr-0.5, and CeO<sub>2</sub>-Zr-1.5 were also prepared.

Crystalline structures of the pristine CeO<sub>2</sub> and CeO<sub>2</sub>-Zr nanostructures before and after calcination processes were analyzed using X-ray diffraction (XRD, Cu K $\alpha$  radiation, D/MAX-2500, Japan). Transmission electron microscope (TEM, JEM-2200FS, Japan) and scanning electron microscope (SEM, Inspect F50, USA) were used to characterize the morphologies of samples. X-ray photoelectron spectroscopy (XPS, Al K $\alpha$  radiation, Kratos Axis-Ultra DLD, UK) was used to analyze the chemical states of elements and surface element composition. The specific Brunauer–Emmett–Teller (BET) surface areas, pore volumes and pore diameter distribution were obtained using

the N<sub>2</sub> adsorption/desorption isotherms of samples, which were measured using nitrogen physisorption apparatus (JW-BK122W, JWGB SCI. TECH. China) at 77 K.

## 2.2 Electrochemical measurement

Zr-doped CeO<sub>2</sub> (16 mg), acetylene black (2 mg) and polytetrafluoro-ethylene (2 mg) were mixed with 1.5 mL ethanol to form a slurry, which was coated onto a clean nickel foam and dried in a vacuum oven at 50 °C overnight. The mass loading of CeO<sub>2</sub>-Zr on a working electrode was about 2 mg cm<sup>-2</sup>. Electrochemical measurements were conducted at room temperature using an electrochemical workstation (CHI 660E, Shanghai Chenhua instrument Co., Ltd.) in 2 M of KOH electrolyte. The electrochemical test including cyclic voltammetry (CV), galvanostatic charge/discharge (GCD) and electrochemical impedance spectroscopy (EIS) were performed using a three electrode cell configuration including a working electrode (Zr-doped CeO<sub>2</sub>/Ni foam electrode), a counter of electrode (platinum foil) and a reference electrode (Hg/HgO electrode).

## 3. Results and discussion

### 3.1 Characterization of pristine CeO<sub>2</sub> and CeO<sub>2</sub>-Zr-1

XRD spectra of the samples of pristine CeO<sub>2</sub> and CeO<sub>2</sub>-Zr-1 are shown in Fig. 1. All the diffraction peaks in these spectra are identified to be (111), (200), (220), (311), (222), (400), (331) and (420) crystal planes of the cubic fluorite phase CeO<sub>2</sub> crystals (JCPDS NO. 34-0394), and no peaks of ZrO<sub>2</sub> are observed in the spectrum of CeO<sub>2</sub>-Zr-1, suggesting that the Zr<sup>4+</sup> ions are doped inside the CeO<sub>2</sub> crystal lattice structure. Because of the similar ionic radii of Zr<sup>4+</sup> (0.072 nm) and Ce<sup>4+</sup> (0.087 nm) ions, some Ce<sup>4+</sup> ions

in the CeO<sub>2</sub> were substituted by Zr<sup>4+</sup> ions to form a substitutional solid solution [37]. After addition of Zr ions, the intensity of CeO<sub>2</sub> peaks becomes decreased and the peaks become broader, indicating the decrease of its crystal sizes. According to the Scherrer formula (1), the average crystallite diameter (L) of these CeO<sub>2</sub> crystallites can be estimated.

$$L = K\lambda / (\beta \cos\theta) \quad (1)$$

where,  $\lambda = 0.15406$  nm,  $K = 0.89$ ,  $\theta$  is the diffracting angle, and  $\beta$  is the half peak width. The obtained average crystallite sizes of CeO<sub>2</sub> and CeO<sub>2</sub>-Zr-1 are 11.5 and 6.7 nm, respectively. The reason why the average crystallite sizes of the CeO<sub>2</sub> decrease after addition of Zr ions is mainly due to the fact that doping of Zr<sup>4+</sup> prevents the fast growth of CeO<sub>2</sub> crystallites during their synthetic process. The smaller nanoparticle sizes mean that there are abundant active sites on the surfaces of these nanoparticles, which are beneficial to the faradaic reactions and can enhance electrochemical performance of the supercapacitor.

Both the pristine CeO<sub>2</sub> and CeO<sub>2</sub>-Zr-1 consist of numerous nanocrystals as shown in Fig. 2 (the TEM images) and SEM images (see Fig. S1, ESI). The obtained average diameters from TEM analysis are about 12.1 nm and 7.1 nm for the pristine CeO<sub>2</sub> and CeO<sub>2</sub>-Zr-1 respectively, which are in good agreements with the results from XRD analysis. The SAED patterns shown in Figs. 2c and 2d clearly demonstrate that both the pristine CeO<sub>2</sub> and CeO<sub>2</sub>-Zr-1 nanocrystals have a cubic fluorite phase structure with good crystallization. From the high resolution (HR)-TEM images shown in Fig. 2b, the lattice spacing of pristine CeO<sub>2</sub> is estimated to be  $\sim 0.329$  nm, which corresponds to the

(111) plane of the cubic fluorite phase CeO<sub>2</sub> crystals. Because of the smaller ionic radius of Zr<sup>4+</sup> (0.072 nm) than that of Ce<sup>4+</sup> (0.087 nm), the Zr<sup>4+</sup> ions occupy the lattice sites of the Ce<sup>4+</sup> ions and form Zr-doped CeO<sub>2</sub> nanocrystals in the synthetic process. Therefore, the CeO<sub>2</sub>-Zr-1 nanocrystals have a smaller lattice spacing (~0.326 nm, shown in Fig. 2e) for the (111) plane of the cubic fluorite phase CeO<sub>2</sub> than that of the pristine CeO<sub>2</sub> nanocrystals.

Fig. 3 shows the N<sub>2</sub> adsorption/desorption isotherm of the pristine CeO<sub>2</sub> and CeO<sub>2</sub>-Zr-1. The typical type-IV adsorption/desorption isotherms with hysteresis loops indicate that both the CeO<sub>2</sub> and CeO<sub>2</sub>-Zr-1 have mesoporous structures in nature [38]. The pore size distributions are centered at ~2.6 nm and ~2.7 nm for the CeO<sub>2</sub> and CeO<sub>2</sub>-Zr-1, respectively (see the insets in the Fig. 3), which clearly proves the formation of mesoporous structures. These mesopores are mainly accumulated at the spaces among numerous nanoparticles. Results showed that both the CeO<sub>2</sub> and CeO<sub>2</sub>-Zr-1 have large pore volumes of 0.2077 cm<sup>3</sup> g<sup>-1</sup> and 0.2108 cm<sup>3</sup> g<sup>-1</sup>. Calculated based on the N<sub>2</sub> adsorption isotherms, the BET surface areas of the CeO<sub>2</sub> and CeO<sub>2</sub>-Zr-1 are 78.2 m<sup>2</sup> g<sup>-1</sup> and 81.0 m<sup>2</sup> g<sup>-1</sup>, respectively. Obviously, both the CeO<sub>2</sub> and CeO<sub>2</sub>-Zr-1 have formed mesoporous nanostructures with large surface areas and pore volumes. Furthermore, results also show that the CeO<sub>2</sub>-Zr-1 has much larger surface areas and pore volumes than those of the pristine CeO<sub>2</sub>. The formation of abundant mesopores is beneficial for the effective ion transport, and the large surface areas provide numerous active sites for the faradaic reactions, both of which can significantly enhance the electrochemical performance of supercapacitors.

Fig. 4a shows the Ce 3d XPS spectra of pristine CeO<sub>2</sub> and CeO<sub>2</sub>-Zr-1. The peaks of Ce 3d<sub>5/2</sub> and Ce 3d<sub>3/2</sub> spin-orbit components are denoted as V and U, respectively. The peaks with symbols of V, V'', V''' and U, U'', U''' are corresponding to those of Ce (IV) 3d<sub>5/2</sub> and 3d<sub>3/2</sub> states, respectively [39]. There are another pairs of peaks of V' and U' in the Ce 3d XPS spectra, which are the characteristics of Ce (III) 3d<sub>5/2</sub> and 3d<sub>3/2</sub> states [40]. Therefore, there are both Ce (IV) and Ce (III) species on the surfaces of both pristine CeO<sub>2</sub> and CeO<sub>2</sub>-Zr-1. Calculated based on the integral peak areas, the obtained percentages of Ce (III) among the total Ce species are 16.1% and 17.7% on the surface, for the pristine CeO<sub>2</sub> and CeO<sub>2</sub>-Zr-1, respectively. The existence of Ce (III) species indicates there are numerous oxygen vacancies generated on the surface of CeO<sub>2</sub> and CeO<sub>2</sub>-Zr-1 nanoparticles [40].

As shown in Fig. 4b, two obvious peaks can be observed in the O 1s XPS spectra of both CeO<sub>2</sub> and CeO<sub>2</sub>-Zr-1. The peak centered at the lower binding energy of 529.4 eV belongs to the lattice oxygen in the CeO<sub>2</sub> crystals, whereas that centered at the higher binding energy of 531.1 eV belongs to the oxygen vacancy [40]. It is obvious that the peak area at 531.1 eV of CeO<sub>2</sub>-Zr-1 is much higher than that of CeO<sub>2</sub>. By calculating the integral ratio of the peak areas, the oxygen vacancy percentage within the total oxygen species on the surface of CeO<sub>2</sub>-Zr-1 is as high as 45.3% on the surface of CeO<sub>2</sub>-Zr-1, and this value is much larger than that of pristine CeO<sub>2</sub> (35.2%), indicating that there are more oxygen vacancies formed on the surface of CeO<sub>2</sub>-Zr-1 than that on the pristine CeO<sub>2</sub>. The abundant oxygen vacancies on the surface can improve the electrical conductivity and enhance the electrochemical reactions [7, 27, 41]. As shown in Fig.

4c, the pairs of peaks at 182.2 and 184.6 eV are attributed to the binding energies of Zr 3d<sub>5/2</sub> and Zr 3d<sub>3/2</sub> characteristic signals, meaning that there are Zr (IV) species on the surface of CeO<sub>2</sub>-Zr-1.

### 3.2 Electrochemical performance of pristine CeO<sub>2</sub> and CeO<sub>2</sub>-Zr electrodes

The cyclic voltammetry (CV) curves at a scan rate of 50 mV s<sup>-1</sup> for both the CeO<sub>2</sub> and CeO<sub>2</sub>-Zr electrodes are shown in Fig 5a. It is obvious that there are a pair of prominently redox peaks for all the CV curves, which are mainly attributed to the reversible conversions of redox reactions between Ce(IV) and Ce(III) [24]. The corresponding chemical reaction can be summarized using the following equation [42]:



There are apparent difference in the closed areas covered by the CV curves, which reveals that the addition of Zr in CeO<sub>2</sub> results in apparent changes of the electrochemical performance. The largest CV integral area of CeO<sub>2</sub>-Zr-1 electrode indicates that it possesses the largest specific capacity than those of the pristine CeO<sub>2</sub>, CeO<sub>2</sub>-Zr-0.5 and CeO<sub>2</sub>-Zr-1.5.

The galvanostatic charge-discharge curves (GCD) of CeO<sub>2</sub> and CeO<sub>2</sub>-Zr-1 within a potential window of 0—0.5 V were measured at a current density of 1 A g<sup>-1</sup> and the results are shown in Fig. 5b. There are obvious potential platforms formed in the charge/discharge processes for all working electrodes due to the Faradaic redox reaction processes [43, 44], which is analogous to that of a battery type material [45][46]. In the discharge process, all the CeO<sub>2</sub>-Zr electrodes show much longer discharge times than that of the pristine CeO<sub>2</sub> electrode, which suggests that the doping of Zr ions in CeO<sub>2</sub>

crystals can effectively enhance the specific capacity. Among them, the CeO<sub>2</sub>-Zr-1 electrode has the longest discharge time, indicating its largest specific capacity.

The specific capacity value  $C$  (C g<sup>-1</sup>) of working electrodes can be calculated based on the following formula [47, 48]:

$$C(\text{C g}^{-1}) = \frac{I \times \Delta t}{m} \quad (3)$$

where,  $I$  (A),  $\Delta t$  (s), and  $m$  (g) are corresponding to the discharge current, the discharge time and the active material mass loading, respectively. The calculated specific capacities are 249.3, 258.4, 448.1 and 287.0 C g<sup>-1</sup> at the discharge current of 1 A g<sup>-1</sup> for pristine CeO<sub>2</sub>, CeO<sub>2</sub>-Zr-0.5, CeO<sub>2</sub>-Zr-1 and CeO<sub>2</sub>-Zr-1.5 electrodes, respectively. Obviously, the doping of Zr ions in CeO<sub>2</sub> crystals significantly enhances the specific capacity of CeO<sub>2</sub> electrode. The CeO<sub>2</sub>-Zr-1 electrode shows the largest specific capacity of 448.1 C g<sup>-1</sup>, which is 1.8 times than that of pristine CeO<sub>2</sub> electrode. For the CeO<sub>2</sub>-Zr-1.5, too many Ce ions were replaced by Zr ions, the involved Ce ions in reversible Faradaic redox reactions significantly decreased. Therefore, CeO<sub>2</sub>-Zr-1.5 electrode shows a less specific capacity than CeO<sub>2</sub>-Zr-1.

Table 1 summarizes the electrochemical performance of CeO<sub>2</sub> based various electrode materials for supercapacitors obtained from literature, and also the CeO<sub>2</sub>-Zr-1 electrode developed in this work. Compared with most of the previously reported pristine CeO<sub>2</sub> electrode materials (including the CeO<sub>2</sub> nanospheres [21], CeO<sub>2</sub> nanowires [21], CeO<sub>2</sub> nanoparticles [26], porous CeO<sub>2</sub> [31] and CeO<sub>2</sub> nanorods [28, 49]) listed in Table 1, the CeO<sub>2</sub>-Zr-1 electrode developed in this work has a larger specific capacity. Although it is reported that the dumbbell CeO<sub>2</sub> [50] and CeO<sub>2</sub> nanobars [51]

presented higher specific capacitance values through addition of a  $\text{K}_4\text{Fe}(\text{CN})_6$  redox-active additives in the KOH electrolyte, their specific capacitance values were only 235 and  $502 \text{ F g}^{-1}$  in the KOH electrolyte without  $\text{K}_4\text{Fe}(\text{CN})_6$  redox-active additive. Furthermore, the specific capacitance of those hybrid  $\text{CeO}_2$  active materials doped with CNTs [1, 32, 52, 53], graphene [23, 54, 55],  $\text{Fe}_2\text{O}_3$  [56],  $\text{CeS}_2$  [57] and NiO [58] are all less than that of the  $\text{CeO}_2$ -Zr-1 electrode in this study. The high specific capacitance of the Zr-doped  $\text{CeO}_2$  can be attributed to its unique nanostructure. Firstly, the abundant mesopores can provide numerous channels for fast electrolyte ion transport and shorten the ion-transport distance. Secondly, its large specific surface area and extraordinary porosity can offer plentiful active sites and provide efficiently contacts between Zr-doped  $\text{CeO}_2$  and electrolyte ions. Thirdly, the abundant oxygen vacancies on the surface of Zr-doped  $\text{CeO}_2$  can improve the electrical conductivity [7, 27, 41]. All of the above can facilitate the faradaic reaction of Zr-doped  $\text{CeO}_2$  electrode material with electrolyte, and thus achieve high specific capacitance [50, 59].

Fig. 5c shows the CV curves of  $\text{CeO}_2$ -Zr-1 electrode measured at 5, 10, 20, 30 and  $50 \text{ mV s}^{-1}$ . With the increase of sweep rate, both the reduction peak and oxidation peak are shifted to the higher and lower potential, respectively, due to the electrode polarization [43, 44]. However, the shapes of these CV curves don't show apparent differences, indicating their good electrochemical reversibility and stability. In addition, the redox peak currents are clearly increased with the increase of scan rates, which indicates the redox reactions at the interfaces between the  $\text{CeO}_2$ -Zr-1 electrode and KOH electrolyte are much faster and more efficient during charge/discharge processes

[60]. The electrodes using CeO<sub>2</sub>, CeO<sub>2</sub>-Zr-0.5 and CeO<sub>2</sub>-Zr-1.5 all exhibit the similar results as shown in Fig. S2.

The GCD curves of CeO<sub>2</sub>-Zr-1 electrode obtained at different charge/discharge current densities from 1 to 10 A g<sup>-1</sup> are shown in Fig. 5d and the other GCD curves for electrodes using CeO<sub>2</sub>, CeO<sub>2</sub>-Zr-0.5 and CeO<sub>2</sub>-Zr-1.5 are shown in Fig. S3. The corresponding specific capacity of all pristine and CeO<sub>2</sub>-Zr electrodes calculated based on the GCD curves are shown in Fig. 5e. It can be seen that the CeO<sub>2</sub>-Zr-1 electrode exhibits much larger capacity than the pristine CeO<sub>2</sub> and other CeO<sub>2</sub>-Zr electrodes even at a high current density of 10 A g<sup>-1</sup>.

Based on the EIS results, Nyquist plots of CeO<sub>2</sub> and CeO<sub>2</sub>-Zr-1 electrodes in the frequency range from 0.01 Hz to 100 kHz are shown in Fig. 5f. The nearly semicircular shape in the high frequency range and the straight line in the low frequency region demonstrate the typical capacitive behavior of CeO<sub>2</sub> and CeO<sub>2</sub>-Zr-1 electrodes [61]. The semicircle curve in Fig. 5f at the high frequency range can be used to obtain the interfacial Faradaic charge transfer resistance (R<sub>ct</sub>) [62]. The calculated R<sub>ct</sub> value (0.48 Ω) of the CeO<sub>2</sub>-Zr-1 electrodes is only 18.8% that of the CeO<sub>2</sub> (2.56 Ω), which means the CeO<sub>2</sub>-Zr-1 electrolyte will show much faster Faradaic redox reactions at the electrode/electrolyte interfaces. Therefore, the CeO<sub>2</sub>-Zr-1 electrode exhibits a larger specific capacity than the pristine CeO<sub>2</sub> electrode.

### **3.3 Electrochemical performance of CeO<sub>2</sub>-Zr-1//AC asymmetric supercapacitor (ASC)**

In order to demonstrate the practical supercapacitor application using the CeO<sub>2</sub>-Zr-1

electrode, an asymmetric supercapacitor (ASC) device was assembled using the CeO<sub>2</sub>-Zr-1 as the positive electrode and activated carbon (AC) as the negative electrode. The ACS device was tested in 2 M KOH electrolyte. To achieve the optimal electrochemical performance, the mass ratio between CeO<sub>2</sub>-Zr-1 and AC was set as 1:2.8, calculated according to the charge balance Equation (4) [61, 63]:

$$\frac{m_+}{m_-} = \frac{C_- \times \Delta V_-}{C_+ \times \Delta V_+} \quad (4)$$

where,  $m$  (mg),  $C$  (F g<sup>-1</sup>), and  $\Delta V$  (V) are the loaded mass, the specific capacitance, and the potential window of CeO<sub>2</sub>-Zr-1 based on positive electrode and AC based on negative electrode, respectively.

Fig. 6a shows the CV curves of the CeO<sub>2</sub>-Zr-1 and AC electrodes measured in a three electrode cell configuration. The potential window of -1~0 V for AC electrode and the potential window of 0~0.6 V for CeO<sub>2</sub>-Zr-1 electrode indicate that the ASC device can work at a potential window from 0 to 1.6 V. Fig. 6b presents the CV curves of the CeO<sub>2</sub>-Zr-1//AC ACS (scan rate: 50 mV s<sup>-1</sup>) at various potential windows in 2M KOH solution. When the operation potential is increased up to 1.6 V, the oxidation and reduction peaks appear, suggesting that the strong redox reactions occur on the surface of the CeO<sub>2</sub>-Zr-1 electrode. Fig. 6c shows the GCD curves measured at 1 A g<sup>-1</sup> at various potential windows from 0.8 to 1.6 V. The shape of GCD curves is well maintained even at a high operating potential of 1.6 V, which proves that the CeO<sub>2</sub>-Zr-1//AC ASC can be successfully operated in the potential window of 0~1.6 V.

Fig. 6d displays the CV behaviors of the assembled CeO<sub>2</sub>-Zr-1//AC ASC at the scan rates from 5 to 50 mV s<sup>-1</sup> and the potential windows of 0~1.6 V. These broad redox

peaks demonstrate the pseudocapacitive behavior of the device. With increase of the scan rates, no obvious change of the shape of CV curves is observed and the redox peaks are similar, revealing the excellent reversible redox reactions occurred at the electrodes.

The GCD curves of the CeO<sub>2</sub>-Zr-1//AC ASC at different current densities are shown in Fig. 6e. Based on the total loading mass of the CeO<sub>2</sub>-Zr-1 and AC, the total specific capacity of the ASC device is calculated to be 97.0 C g<sup>-1</sup> at a current density of 1 A g<sup>-1</sup>. It is 56.8 C g<sup>-1</sup> at the increased current density of 8 A g<sup>-1</sup> as shown in Fig. 6f, revealing a good rate capacity of the CeO<sub>2</sub>-Zr-1//AC ASC device. The energy density (E, Wh kg<sup>-1</sup>) and power density (P, W kg<sup>-1</sup>) can be calculated based on the GCD curves according to the following equations [64, 65]:

$$E = \frac{0.5C \times \Delta V}{3.6} \quad (5)$$

$$P = \frac{3600E}{\Delta t} \quad (6)$$

I which  $C$  (C g<sup>-1</sup>) is the total specific capacity of ASC device,  $\Delta V$  (V) is the potential window during the charge–discharge test,  $\Delta t$  (s) is the discharge time. Fig. 7a shows the Ragone plots (energy density vs. power density) of CeO<sub>2</sub>-Zr-1//AC ACS. The ASC device exhibits a maximum energy density of 23.3 Wh kg<sup>-1</sup> and a power density 398.5 W kg<sup>-1</sup> at a current density of 1 A g<sup>-1</sup>. Even at the high power density of 6080 W kg<sup>-1</sup>, it still remains a high energy density of 11.99 Wh kg<sup>-1</sup>, which demonstrates the good power capability of CeO<sub>2</sub>-Zr-1//AC ACS. Remarkably, compared with other CeO<sub>2</sub> based ASCs reported in the literature as illustrated in the Fig. 7a, the energy and power densities of CeO<sub>2</sub>-Zr-1//AC device in this study are much higher, e.g., better than those

of CeO<sub>2</sub> nanorods (5.1 Wh/kg at 250 W/kg) [66], CeO<sub>2</sub>/CeS<sub>2</sub> (21.2 Wh/kg at 303 W/kg) [57] and CeO<sub>2</sub> nanoparticles (12.68 Wh/kg at 100 W/kg) [27]. Furthermore, the electrochemical performance of this CeO<sub>2</sub>-Zr-1//AC ASC device is superior to those of many transition metal oxides based ASC devices, such as MnO<sub>2</sub>@Ni//AC (7.66 Wh kg<sup>-1</sup> at 600 W kg<sup>-1</sup>) [67], Mn<sub>3</sub>O<sub>4</sub>/Ni(OH)<sub>2</sub>//AC (15.3 Wh kg at 168.8 W kg<sup>-1</sup>) [68], NiO-Au//AC (18 Wh kg at 350 W kg<sup>-1</sup>) [69], MnO<sub>2</sub>//AC (18.2 Wh kg at 200 W kg<sup>-1</sup>) [70].

The cycling stability of CeO<sub>2</sub>-Zr-1//AC ACS device was measured up to 6000 cycles by continuous charging-discharging at 6 A g<sup>-1</sup>, and the corresponding total specific capacity are shown in Fig. 7b. After 6000 cycles, the specific capacity remains 96.4% of its initial value, demonstrating an outstanding long-term cycling stability. The formation of mesoporous nanostructure and the reduced size of nanocrystals of CeO<sub>2</sub>-Zr-1 can effectively accommodate the volume change of nanoparticles during the charge/discharge cycle processes [41]. Therefore, the CeO<sub>2</sub>-Zr-1 is a good electrode material to fabricate ASC devices with a high power density and outstanding long-term cycling stability.

#### **4. Conclusion**

In brief, mesoporous Zr-doped CeO<sub>2</sub> nanostructures were synthesized using a convenient hydrothermal method and an assisted calcination process for high-performance supercapacitor application. The CeO<sub>2</sub>-Zr-1 exhibits a specific capacity of 448.1 C g<sup>-1</sup> at the current density of 1 A g<sup>-1</sup> in the 2M KOH electrolyte, which is almost 1.8 times higher than that of pristine CeO<sub>2</sub>. The CeO<sub>2</sub>-Zr-1//AC ACS device exhibits a high energy value of 23.3 at a power density of 398.5 W kg<sup>-1</sup>. In addition, the ASC

device shows an outstanding long-term cycling stability with 96.4% capacity retention even after 6000 cycles. The good electrochemical performance of the CeO<sub>2</sub>-Zr-1 electrode material can be attributed to the extraordinary porosity, small nanocrystal size and large surface area. Therefore, the mesoporous Zr-doped CeO<sub>2</sub> nanostructures electrode material has good application promise in supercapacitor and energy storage device.

## Supporting Information

Fig. S1: SEM image of (a) pristine CeO<sub>2</sub> and (b) CeO<sub>2</sub>-Zr-1 samples. Fig. S2: CV curves measured at multiple scan rates: (a) CeO<sub>2</sub>, (b) CeO<sub>2</sub>-Zr-0.5 and (c) CeO<sub>2</sub>-Zr-1.5 electrodes. Fig. S3: GCD profiles at different current densities: (a) CeO<sub>2</sub>, (b) CeO<sub>2</sub>-Zr-0.5 and (c) CeO<sub>2</sub>-Zr-1.5 electrodes.

## Conflicts of interest

There are no conflicts to declare.

## Acknowledgments

This work is supported by the Funding from UK Engineering Physics and Science Research Council (EPSRC EP/P018998/1), Newton Mobility Grant (IE161019) through Royal Society and NFSC, and Royal academy of Engineering UK-Research Exchange with China and India are also acknowledged.

## References

- [1] Z.-J. Sun, H. Ge, S. Zhu, X.-M. Cao, X. Guo, Z.-H. Xiu, Z.-H. Huang, H. Li, T. Ma, X.-M. Song, Versatile template-free construction of hollow nanostructured CeO<sub>2</sub> induced by functionalized carbon materials, *J. Mater. Chem. A*, 7 (2019) 12008-12017.
- [2] Y. Liu, G. Jiang, S. Sun, B. Xu, J. Zhou, Y. Zhang, J. Yao, Decoration of carbon nanofibers with NiCo<sub>2</sub>S<sub>4</sub> nanoparticles for flexible asymmetric supercapacitors, *J. Alloys Compd.*, 731 (2018) 560-568.

- [3] G. Zhang, X. Xiao, B. Li, P. Gu, H. Xue, H. Pang, Transition metal oxides with one-dimensional/one-dimensional-analogue nanostructures for advanced supercapacitors, *J. Mater. Chem. A*, 5 (2017) 8155-8186.
- [4] W. Xu, J. Wan, W. Huo, Q. Yang, Y. Li, C. Zhang, X. Gu, C. Hu, Sodium ions pre-intercalation stabilized tunnel structure of  $\text{Na}_2\text{Mn}_8\text{O}_{16}$  nanorods for supercapacitors with long cycle life, *Chem. Eng. J.*, 354 (2018) 1050-1057.
- [5] R.S. Kate, S.A. Khalate, R.J. Deokate, Overview of nanostructured metal oxides and pure nickel oxide (NiO) electrodes for supercapacitors: A review, *J. Alloys Compd.*, 734 (2018) 89-111.
- [6] B.S. Shen, X. Zhang, R.S. Guo, J.W. Lang, J.T. Chen, X.B. Yan, Carbon encapsulated  $\text{RuO}_2$  nano-dots anchoring on graphene as an electrode for asymmetric supercapacitors with ultralong cycle life in an ionic liquid electrolyte, *J. Mater. Chem. A*, 4 (2016) 8180-8189.
- [7] K. Xiang, Z.C. Xu, T.T. Qu, Z.F. Tian, Y. Zhang, Y.Z. Wang, M.J. Xie, X.K. Guo, W.P. Ding, X.F. Guo, Two dimensional oxygen-vacancy-rich  $\text{Co}_3\text{O}_4$  nanosheets with excellent supercapacitor performances, *Chem. Commun.*, 53 (2017) 12410-12413.
- [8] S. Raj, S.K. Srivastava, P. Kar, P. Roy, In situ growth of  $\text{Co}_3\text{O}_4$  nanoflakes on reduced graphene oxide-wrapped Ni-foam as high performance asymmetric supercapacitor, *Electrochim. Acta*, 302 (2019) 327-337.
- [9] K.H. Han, H. Huang, Q.H. Gong, T.T. Si, Z.L. Zhang, G.W. Zhou, Temperature-induced hierarchical Tremella-like and Pinecone-like NiO microspheres for high-performance supercapacitor electrode materials, *J. Mater. Sci.*, 53 (2018) 12477-12491.
- [10] Z. Gonzalez, B. Ferrari, A.J. Sanchez-Herencia, A. Caballero, J. Morales, Use of Polyelectrolytes for the Fabrication of Porous NiO Films by Electrophoretic Deposition for Supercapacitor Electrodes, *Electrochim. Acta*, 211 (2016) 110-118.
- [11] J.G. Wang, F.Y. Kang, B.Q. Wei, Engineering of  $\text{MnO}_2$ -based nanocomposites for high-performance supercapacitors, *Prog. Mater. Sci.*, 74 (2015) 51-124.
- [12] P.B. Liu, Y.D. Zhu, X.G. Gao, Y. Huang, Y. Wang, S.Y. Qin, Y.Q. Zhang, Rational construction of bowl-like  $\text{MnO}_2$  nanosheets with excellent electrochemical performance for supercapacitor electrodes, *Chem. Eng. J.*, 350 (2018) 79-88.
- [13] P.K. Singh, A.K. Das, G. Hatui, G.C. Nayak, Shape controlled green synthesis of  $\text{CuO}$  nanoparticles through ultrasonic assisted electrochemical discharge process and its application for supercapacitor, *Mater. Chem. Phys.*, 198 (2017) 16-34.
- [14] X.D. Hong, S.L. Li, R. Wang, J.W. Fu, Hierarchical  $\text{SnO}_2$  nanoclusters wrapped functionalized carbonized cotton cloth for symmetrical supercapacitor, *J. Alloys Compd.*, 775 (2019) 15-21.
- [15] V. Bonu, B. Gupta, S. Chandra, A. Das, S. Dhara, A.K. Tyagi, Electrochemical supercapacitor performance of  $\text{SnO}_2$  quantum dots, *Electrochim. Acta*, 203 (2016) 230-237.
- [16] B. Balamuralitharan, I.H. Cho, J.S. Bak, H.J. Kim,  $\text{V}_2\text{O}_5$  nanorod electrode material for enhanced electrochemical properties by a facile hydrothermal method for supercapacitor applications, *New J. Chem.*, 42 (2018) 11862-11868.
- [17] J.Y. Ma, X.T. Guo, Y. Yan, H.G. Xue, H. Pang,  $\text{FeO}_x$ -Based Materials for Electrochemical Energy Storage, *Adv. Sci.*, 5 (2018) 1700986.

- [18] V.D. Nithya, N.S. Arul, Progress and development of Fe<sub>3</sub>O<sub>4</sub> electrodes for supercapacitors, *J. Mater. Chem. A*, 4 (2016) 10767-10778.
- [19] V.D. Nithya, N.S. Arul, Review on alpha-Fe<sub>2</sub>O<sub>3</sub> based negative electrode for high performance supercapacitors, *J. Power Sources*, 327 (2016) 297-318.
- [20] C.C. Raj, R. Prasanth, Review-Advent of TiO<sub>2</sub> Nanotubes as Supercapacitor Electrode, *J. Electrochem. Soc.*, 165 (2018) E345-E358.
- [21] L. Wang, Y. Li, M. Shi, W. Ma, H. Cui, Synthesis of CeO<sub>2</sub> nanocrystals with controlled size and shape and their influence on electrochemical performance, *J. Sol-Gel Sci. Technol.*, 83 (2017) 308-314.
- [22] A. Jeyaranjan, T.S. Sakthivel, M. Molinari, D.C. Sayle, S. Seal, Morphology and Crystal Planes Effects on Supercapacitance of CeO<sub>2</sub> Nanostructures: Electrochemical and Molecular Dynamics Studies, *Part. Part. Syst. Charact.*, 35 (2018).
- [23] T. Saravanan, M. Shanmugam, P. Anandan, M. Azhagurajan, K. Pazhanivel, M. Arivanandhan, Y. Hayakawa, R. Jayavel, Facile synthesis of graphene-CeO<sub>2</sub> nanocomposites with enhanced electrochemical properties for supercapacitors, *Dalton T.*, 44 (2015) 9901-9908.
- [24] N. Maheswari, G. Muralidharan, Hexagonal CeO<sub>2</sub> nanostructures: an efficient electrode material for supercapacitors, *Dalton T.*, 45 (2016) 14352-14362.
- [25] X. Meng, C. Wan, X. Jiang, X. Ju, Rodlike CeO<sub>2</sub>/carbon nanocomposite derived from metal-organic frameworks for enhanced supercapacitor applications, *J. Mater. Sci.*, 53 (2018) 13966-13975.
- [26] R. Murugan, G. Ravi, R. Yuvakkumar, S. Rajendran, N. Maheswari, G. Muralidharan, Y. Hayakawa, Pure and Co doped CeO<sub>2</sub> nanostructure electrodes with enhanced electrochemical performance for energy storage applications, *Ceram. Int.*, 43 (2017) 10494-10501.
- [27] M. Kumar, J.-H. Yun, V. Bhatt, B. Singh, J. Kim, J.-S. Kim, B.S. Kim, C.Y. Lee, Role of Ce<sup>3+</sup> valence state and surface oxygen vacancies on enhanced electrochemical performance of single step solvothermally synthesized CeO<sub>2</sub> nanoparticles, *Electrochim. Acta*, 284 (2018) 709-720.
- [28] H. Wang, M. Liang, X. Zhang, D. Duan, W. Shi, Y. Song, Z. Sun, Novel CeO<sub>2</sub> nanorod framework prepared by dealloying for supercapacitors applications, *Ionics*, 24 (2018) 2063-2072.
- [29] N. Padmanathan, S. Selladurai, Shape controlled synthesis of CeO<sub>2</sub> nanostructures for high performance supercapacitor electrodes, *RSC Adv.*, 4 (2014) 6527-6534.
- [30] R. Murugan, G. Ravi, G. Vijayaprasath, S. Rajendran, M. Thaiyan, M. Nallappan, M. Gopalan, Y. Hayakawa, Ni-CeO<sub>2</sub> spherical nanostructures for magnetic and electrochemical supercapacitor applications, *Phys. Chem. Chem. Phys.*, 19 (2017) 4396-4404.
- [31] K. Prasanna, P. Santhoshkumar, Y.N. Jo, I.N. Sivagami, S.H. Kang, Y.C. Joe, C.W. Lee, Highly porous CeO<sub>2</sub> nanostructures prepared via combustion synthesis for supercapacitor applications, *Appl. Surf. Sci.*, 449 (2018) 454-460.
- [32] D. Deng, N. Chen, Y. Li, X. Xing, X. Liu, X. Xiao, Y. Wang, Cerium oxide nanoparticles/multi-wall carbon nanotubes composites: Facile synthesis and electrochemical performances as supercapacitor electrode materials, *Phys. E.*, 86 (2017)

284-291.

[33] W. Raza, F. Ali, N. Raza, Y. Luo, K.-H. Kim, J. Yang, S. Kumar, A. Mehmood, E.E. Kwon, Recent advancements in supercapacitor technology, *Nano Energy*, 52 (2018) 441-473.

[34] J. Xie, P. Yang, Y. Wang, T. Qi, Y. Lei, C.M. Li, Puzzles and confusions in supercapacitor and battery: Theory and solutions, *J. Power Sources*, 401 (2018) 213-223.

[35] H. Li, Z. Li, Z. Wu, M. Sun, S. Han, C. Cai, W. Shen, X. Liu, Y. Fu, Enhanced electrochemical performance of CuCo<sub>2</sub>S<sub>4</sub>/carbon nanotubes composite as electrode material for supercapacitors, *J. Colloid Interf. Sci.*, 549 (2019) 105-113.

[36] W. Xu, Z. Jiang, Q. Yang, W. Huo, M.S. Javed, Y. Li, L. Huang, X. Gu, C. Hu, Approaching the lithium-manganese oxides' energy storage limit with Li<sub>2</sub>MnO<sub>3</sub> nanorods for high-performance supercapacitor, *Nano Energy*, 43 (2018) 168-176.

[37] Z. Li, J. Wang, S. Zhang, S. Yan, B. Cao, W. Shen, Z. Wang, Y.Q. Fu, Highly sensitive NH<sub>3</sub> gas sensor based on the porous Ce<sub>0.94</sub>Zr<sub>0.06</sub>O<sub>2</sub> nano-sheets with ppb level detection limit, *J. Alloy. Compd.*, 742 (2018) 712-720.

[38] Z. Li, H. Li, Z. Wu, M. Wang, J. Luo, H. Torun, P. Hu, C. Yang, M. Grundmann, X. Liu, Y. Fu, Advances in designs and mechanisms of semiconducting metal oxide nanostructures for high-precision gas sensors operated at room temperature, *Mater. Horiz.*, 6 (2019) 470-506.

[39] J. Wang, Z. Li, S. Zhang, S. Yan, B. Cao, Z. Wang, Y. Fu, Enhanced NH<sub>3</sub> gas-sensing performance of silica modified CeO<sub>2</sub> nanostructure based sensors, *Sensors and Actuators B-Chemical*, 255 (2018) 862-870.

[40] C. Wang, C. Zhang, W. Hua, Y. Guo, G. Lu, S. Gil, A. Giroir-Fendler, Catalytic oxidation of vinyl chloride emissions over Co-Ce composite oxide catalysts, *Chem. Eng. J.*, 315 (2017) 392-402.

[41] Z. Fang, S.U. Rehman, M. Sun, Y. Yuan, S. Jin, H. Bi, Hybrid NiO-CuO mesoporous nanowire array with abundant oxygen vacancies and a hollow structure as a high-performance asymmetric supercapacitor, *J. Mater. Chem. A*, 6 (2018) 21131-21142.

[42] S. Maiti, A. Pramanik, S. Mahanty, Extraordinarily high pseudocapacitance of metal organic framework derived nanostructured cerium oxide, *Chem. Commun.*, 50 (2014) 11717-11720.

[43] L. Wang, M. Arif, G. Duan, S. Chen, X. Liu, A high performance quasi-solid-state supercapacitor based on CuMnO<sub>2</sub> nanoparticles, *J. Power Sources*, 355 (2017) 53-61.

[44] H. Li, Z. Li, Z. Wu, M. Sun, S. Han, C. Cai, W. Shen, Y. Fu, Nanocomposites of Cobalt Sulfide Embedded Carbon Nanotubes with Enhanced Supercapacitor Performance, *J. Electrochem. Soc.*, 166 (2019) A1031-A1037.

[45] Thierry Brousse, Daniel Belanger, J.W. Longd, To Be or Not To Be Pseudocapacitive?, *J. Electrochem. Soc.*, (2015) A5185-A5189

[46] B.E. Conway, *Electrochemical Capacitors: Scientific Fundamentals and Technology Applications*, Kluwer Academic/Plenum Publishers, New-York, (1999).

[47] S.K. Shinde, M.B. Jalak, S.Y. Kim, H.M. Yadav, G.S. Ghodake, A.A. Kadam, D.Y. Kim, Effect of Mn doping on the chemical synthesis of interconnected nanoflakes-like

- CoS thin films for high performance supercapacitor applications, *Ceram. Int.*, 44 (2018) 23102-23108.
- [48] D.Y. Kim, G.S. Ghodake, N.C. Maile, A.A. Kadam, D. Sung Lee, V.J. Fulari, S.K. Shinde, Chemical synthesis of hierarchical NiCo<sub>2</sub>S<sub>4</sub> nanosheets like nanostructure on flexible foil for a high performance supercapacitor, *Sci. Rep.*, 7 (2017) 9764.
- [49] A. Jeyaranjan, T.S. Sakthivel, M. Molinari, D.C. Sayle, S. Seal, Morphology and Crystal Planes Effects on Supercapacitance of CeO<sub>2</sub> Nanostructures: Electrochemical and Molecular Dynamics Studies, *Part. Part. Syst. Charact.*, 35 (2018) 1800176.
- [50] G. Zeng, Y. Chen, L. Chen, P. Xiong, M. Wei, Hierarchical cerium oxide derived from metal-organic frameworks for high performance supercapacitor electrodes, *Electrochim. Acta*, 222 (2016) 773-780.
- [51] S. Maiti, A. Pramanik, S. Mahanty, Extraordinarily high pseudocapacitance of metal organic framework derived nanostructured cerium oxide, *Chem. Commun. (Camb)*, 50 (2014) 11717-11720.
- [52] R.S. Kalubarme, Y.H. Kim, C.J. Park, One step hydrothermal synthesis of a carbon nanotube/cerium oxide nanocomposite and its electrochemical properties, *Nanotechnology*, 24 (2013) 365401.
- [53] Y. Luo, T. Yang, Q. Zhao, M. Zhang, CeO<sub>2</sub>/CNTs hybrid with high performance as electrode materials for supercapacitor, *J. Alloys Compd.*, 729 (2017) 64-70.
- [54] T. Li, H. Liu, A simple synthesis method of nanocrystals CeO<sub>2</sub> modified rGO composites as electrode materials for supercapacitors with long time cycling stability, *Powder Technol.*, 327 (2018) 275-281.
- [55] H. Heydari, M.B. Gholivand, A novel high-performance supercapacitor based on high-quality CeO<sub>2</sub>/nitrogen-doped reduced graphene oxide nanocomposite, *Appl. Phys. A*, 123 (2017) 187.
- [56] N.S. Arul, D. Mangalaraj, R. Ramachandran, A.N. Grace, J.I. Han, Fabrication of CeO<sub>2</sub>/Fe<sub>2</sub>O<sub>3</sub> composite nanospindles for enhanced visible light driven photocatalysts and supercapacitor electrodes, *J. Mater. Chem. A*, 3 (2015) 15248-15258.
- [57] N. Bibi, Y. Xia, S. Ahmed, Y. Zhu, S. Zhang, A. Iqbal, Highly stable mesoporous CeO<sub>2</sub>/CeS<sub>2</sub> nanocomposite as electrode material with improved supercapacitor electrochemical performance, *Ceram. Int.*, 44 (2018) 22262-22270.
- [58] N. Padmanathan, S. Selladurai, Electrochemical capacitance of porous NiO–CeO<sub>2</sub> binary oxide synthesized via sol–gel technique for supercapacitor, *Ionics*, 20 (2013) 409-420.
- [59] A. Xie, F. Tao, T. Li, L. Wang, S. Chen, S. Luo, C. Yao, Graphene-cerium oxide/porous polyaniline composite as a novel electrode material for supercapacitor, *Electrochim. Acta*, 261 (2018) 314-322.
- [60] L. Li, X. Liu, C. Liu, H. Wan, J. Zhang, P. Liang, H. Wang, H. Wang, Ultra-long life nickel nanowires@nickel-cobalt hydroxide nanoarrays composite pseudocapacitive electrode: Construction and activation mechanism, *Electrochim. Acta*, 259 (2018) 303-312.
- [61] S. Liu, S.C. Jun, Hierarchical manganese cobalt sulfide core-shell nanostructures for high-performance asymmetric supercapacitors, *J. Power Sources*, 342 (2017) 629-637.

- [62] A.S. Dezfuli, M.R. Ganjali, H.R. Naderi, P. Norouzi, A high performance supercapacitor based on a ceria/graphene nanocomposite synthesized by a facile sonochemical method, *RSC Adv.*, 5 (2015) 46050-46058.
- [63] Y. Liu, Q. Lu, Z. Huang, S. Sun, B. Yu, U. Evariste, G. Jiang, J. Yao, Electrodeposition of Ni-Co-S nanosheet arrays on N-doped porous carbon nanofibers for flexible asymmetric supercapacitors, *J. Alloys Compd.*, 762 (2018) 301-311.
- [64] C. Li, J. Balamurugan, T. Tran Duy, N.H. Kim, J.H. Lee, 3D hierarchical CoO@MnO<sub>2</sub> core-shell nanohybrid for high-energy solid state asymmetric supercapacitors, *J. Mater. Chem. A*, 5 (2017) 397-408.
- [65] H. Li, Z. Li, M. Sun, Z. Wu, W. Shen, Y.Q. Fu, Zinc cobalt sulfide nanoparticles as high performance electrode material for asymmetric supercapacitor, *Electrochim. Acta*, 319 (2019) 716-726.
- [66] G. He, H. Fan, L. Ma, K. Wang, C. Liu, D. Ding, L. Chen, Dumbbell-like ZnO nanoparticles-CeO<sub>2</sub> nanorods composite by one-pot hydrothermal route and their electrochemical charge storage, *Appl. Surf. Sci.*, 366 (2016) 129-138.
- [67] Y.-C. Tsai, W.-D. Yang, K.-C. Lee, C.-M. Huang, An Effective Electrodeposition Mode for Porous MnO<sub>2</sub>/Ni Foam Composite for Asymmetric Supercapacitors, *Materials*, 9 (2016) 246.
- [68] Q.-Q. He, H.-Y. Wang, N. Lun, Y.-X. Qi, J.-R. Liu, J.-K. Feng, J. Qiu, Y.J. Bai, Fabricating a Mn<sub>3</sub>O<sub>4</sub>/Ni(OH)<sub>2</sub> Nanocomposite by Water-Boiling Treatment for Use in Asymmetric Supercapacitors as an Electrode Material, *ACS Sustainable Chem. Eng.*, 6 (2018) 15688-15696.
- [69] Y. Tan, Y. Li, L. Kong, L. Kang, F. Ran, Synthesis of ultra-small gold nanoparticles decorated onto NiO nanobelts and their high electrochemical performance, *Dalton T.*, 47 (2018) 8078-8086.
- [70] C.C.H. Tran, J. Santos-Pena, C. Damas, Theoretical and Practical Approach of Soft Template Synthesis for the Preparation of MnO<sub>2</sub> Supercapacitor Electrode, *J. Phys. Chem. C*, 122 (2018) 16-29.
- [71] N. Maheswari, G. Muralidharan, Supercapacitor Behavior of Cerium Oxide Nanoparticles in Neutral Aqueous Electrolytes, *Energy Fuels*, 29 (2015) 8246-8253.
- [72] M. Vanitha, Keerthi, P. Cao, N. Balasubramanian, Ag nanocrystals anchored CeO<sub>2</sub>/graphene nanocomposite for enhanced supercapacitor applications, *J. Alloys Compd.*, 644 (2015) 534-544.
- [73] Q. Gong, Y. Li, H. Huang, J. Zhang, T. Gao, G. Zhou, Shape-controlled synthesis of Ni-CeO<sub>2</sub>@PANI nanocomposites and their synergetic effects on supercapacitors, *Chem. Eng. J.*, 344 (2018) 290-298.

## Table Caption

Table 1 Summary of the electrochemical performance of CeO<sub>2</sub> based electrode materials for supercapacitors.

## Figure Captions

Fig. 1 XRD spectra of the pristine CeO<sub>2</sub> and CeO<sub>2</sub>-Zr-1.

Fig. 2 (a) TEM, (b) HRTEM images and (c) SAED of pristine CeO<sub>2</sub>; (d) TEM, (e) HRTEM images and (f) SAED of CeO<sub>2</sub>-Zr-1.

Fig. 3 N<sub>2</sub> adsorption isotherms and pore size distributions of (a) pristine CeO<sub>2</sub> and (b) CeO<sub>2</sub>-Zr-1.

Fig. 4 (a) Ce 3d, (b) O 1s XPS spectra of pristine CeO<sub>2</sub> and CeO<sub>2</sub>-Zr-1, (c) Zr 3d XPS spectrum of CeO<sub>2</sub>-Zr-1.

Fig. 5 (a) CV curves at a scan rate of 50 mV s<sup>-1</sup> and (b) GCD curves at a current density of 1 A g<sup>-1</sup> for the CeO<sub>2</sub>, CeO<sub>2</sub>-Zr-0.5, CeO<sub>2</sub>-Zr-1 and CeO<sub>2</sub>-Zr-1.5 electrodes, (c) CV curves measured at multiple scan rates and (d) GCD profiles at different current densities for the CeO<sub>2</sub>-Zr-1 electrodes, (e) specific capacity at various current densities of the CeO<sub>2</sub>, CeO<sub>2</sub>-Zr-0.5, CeO<sub>2</sub>-Zr-1 and CeO<sub>2</sub>-Zr-1.5 electrodes and (f) EIS Nyquist plots for the CeO<sub>2</sub>, and CeO<sub>2</sub>-Zr-1 electrodes (the potential vs (Hg/HgO) is 0.5 V). (Inset: the magnified section at high frequency region).

Fig. 6 (a) CV curves of AC and CeO<sub>2</sub>-Zr-1 electrodes measured in three electrode system at a scan rate of 10 mV s<sup>-1</sup>; (b) CV curves (scan rate: 50 mV s<sup>-1</sup>) and (c) GCD curves (current density: 1 A g<sup>-1</sup>) of the CeO<sub>2</sub>-Zr-1//AC ACS at different

potential windows; (d) CV curves of the CeO<sub>2</sub>-Zr-1//AC ACS device at various scan rates, (e) GCD curves and (f) corresponding specific capacity of the CeO<sub>2</sub>-Zr-1//AC ACS at different current densities.

Fig. 7 (a) Ragone plot of the CeO<sub>2</sub>-Zr-1//AC ACS device (energy density vs power density) and comparison with those reported devices in the literature, (b) Cycling stability of the CeO<sub>2</sub>-Zr-1//AC ACS device at 6 A g<sup>-1</sup>.

Table 1 Summary of the electrochemical performance of CeO<sub>2</sub> based electrode materials for supercapacitors.

Electrode materials	Current density or scan rates	Specific capacity	Potential window (V)	Electrolyte	Ref.
CeO <sub>2</sub> nanorods	1 A g <sup>-1</sup>	162.47 F g <sup>-1</sup>	-0.1-0.45	3M KOH	[49]
Porous CeO <sub>2</sub>	1 A g <sup>-1</sup>	134.6 F g <sup>-1</sup>	0-0.45	1M KOH	[31]
CeO <sub>2</sub> nanorods	1 A g <sup>-1</sup>	149.5 F g <sup>-1</sup>	0.05-0.5	2M KOH	[28]
CeO <sub>2</sub> nanospheres	6.3 A g <sup>-1</sup>	372.6 F g <sup>-1</sup>	0-0.45	3M KOH	[21]
CeO <sub>2</sub> nanoparticles	0.25 A g <sup>-1</sup>	142.5 F g <sup>-1</sup>	0-0.8	1M Na <sub>2</sub> SO <sub>4</sub>	[27]
Hexagonal CeO <sub>2</sub>	2 A g <sup>-1</sup>	457 F g <sup>-1</sup>	0-0.8	NaCl	[71]
Carbon coated CeO <sub>2</sub> nanorods	0.5 A g <sup>-1</sup>	644 F g <sup>-1</sup>	0-0.35	3M KOH	[29]
Hexagonal CeO <sub>2</sub> /CNTs	5mA cm <sup>-2</sup>	289 F g <sup>-1</sup>	0-2	0.5M Na <sub>2</sub> SO <sub>4</sub>	[52]
CeO <sub>2</sub> nanoparticles/MCNTs	1 A g <sup>-1</sup>	455.6 F g <sup>-1</sup>	0-0.45	6M KOH	[32]
CeO <sub>2</sub> chunks/CNTs	1mV s <sup>-1</sup>	818 F g <sup>-1</sup>	0.3-0.81	2M KOH	[53]
Hollow sphere CeO <sub>2</sub> /MCNTs	0.5 A g <sup>-1</sup>	450.5 F g <sup>-1</sup>	0-0.5	6M KOH	[1]
Graphene/CeO <sub>2</sub> nanocrystals	10 mV s <sup>-1</sup>	110 F g <sup>-1</sup>	-0.3-1.0	1M H <sub>2</sub> SO <sub>4</sub>	[23]
RGO/CeO <sub>2</sub> -PANI	1 A g <sup>-1</sup>	454.8 F g <sup>-1</sup>	0-0.6	0.5M H <sub>2</sub> SO <sub>4</sub>	[59]
CeO <sub>2</sub> nanocrystals/RGO	2 A g <sup>-1</sup>	282 F g <sup>-1</sup>	0-0.5	3M KOH	[54]
CeO <sub>2</sub> /N-RGO	2mV s <sup>-1</sup>	230 F g <sup>-1</sup>	-0.2-0.5	6M KOH	[55]
Ag/CeO <sub>2</sub> /RGO	0.2 A g <sup>-1</sup>	710.42 F g <sup>-1</sup>	-0.3-1.0	3M KOH	[72]
Porous NiO-CeO <sub>2</sub>	1 A g <sup>-1</sup>	305 F g <sup>-1</sup>	0-0.45	3M KOH	[58]
CeO <sub>2</sub> /Fe <sub>2</sub> O <sub>3</sub> nanospindles	5mV s <sup>-1</sup>	142.6 F g <sup>-1</sup>	-0.3-0.3	6MKOH	[56]
Mesoporous CeO <sub>2</sub> /CeS <sub>2</sub>	1 A g <sup>-1</sup>	420 F g <sup>-1</sup>	0-0.5	0.1M KOH	[57]
Ni-CeO <sub>2</sub> nanospheres	1 A g <sup>-1</sup>	201 F g <sup>-1</sup>	-0.2-0.8	1M Na <sub>2</sub> SO <sub>4</sub>	[73]

Co-CeO <sub>2</sub> nanoparticles	2 A g <sup>-1</sup>	573 F g <sup>-1</sup>	0-0.45	1M KOH	[26]
Ni-CeO <sub>2</sub> nanoparticles	2 A g <sup>-1</sup>	577 F g <sup>-1</sup>	0-0.45	1M KOH	[30]
Mesoporous CeO <sub>2</sub> -Zr-1	1 A g <sup>-1</sup>	448.1 C g <sup>-1</sup> (905.4 F g <sup>-1</sup> )	0-0.5	2M KOH	This work

---

Note: PANI: polyaniline; CNTs: carbon nanotubes; RGO: reduced graphene oxide

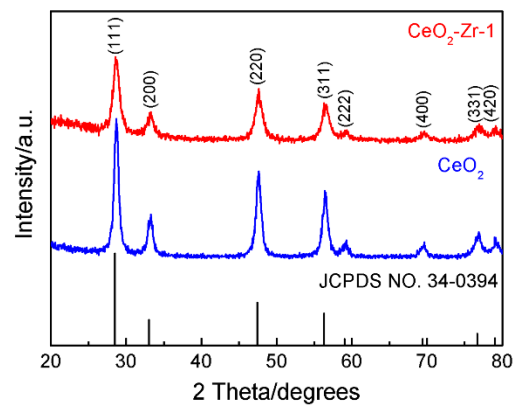


Fig. 1 XRD spectra of the pristine CeO<sub>2</sub> and CeO<sub>2</sub>-Zr-1

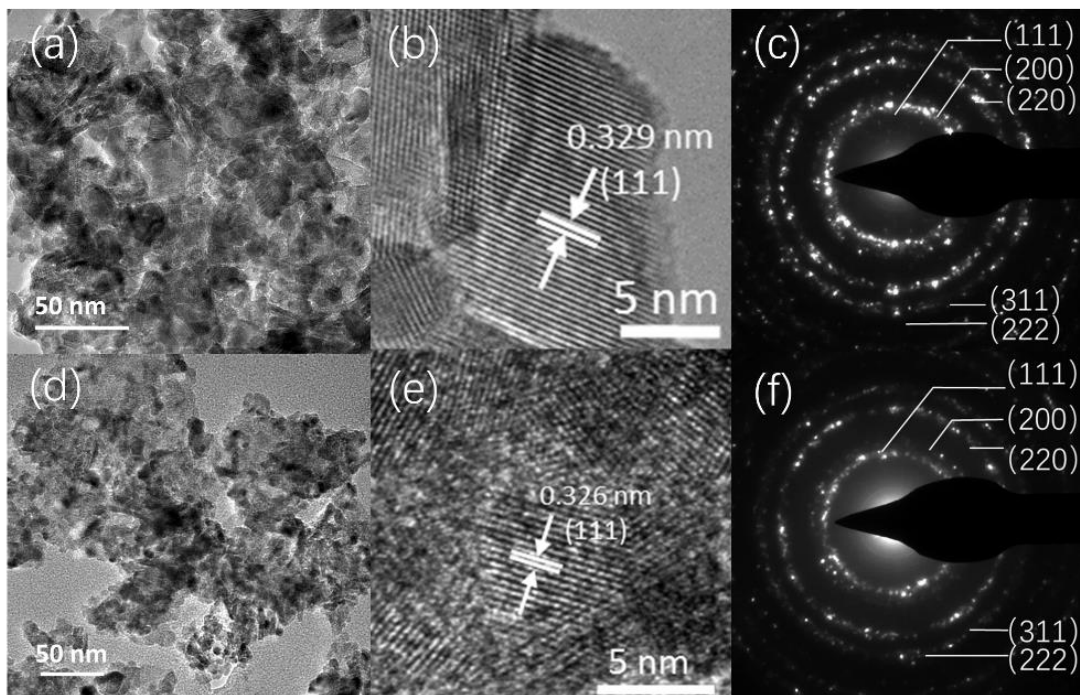


Fig. 2 (a) TEM, (b) HRTEM images and (c) SAED of pristine CeO<sub>2</sub>; (d) TEM, (e) HRTEM images and (f) SAED of CeO<sub>2</sub>-Zr-1.

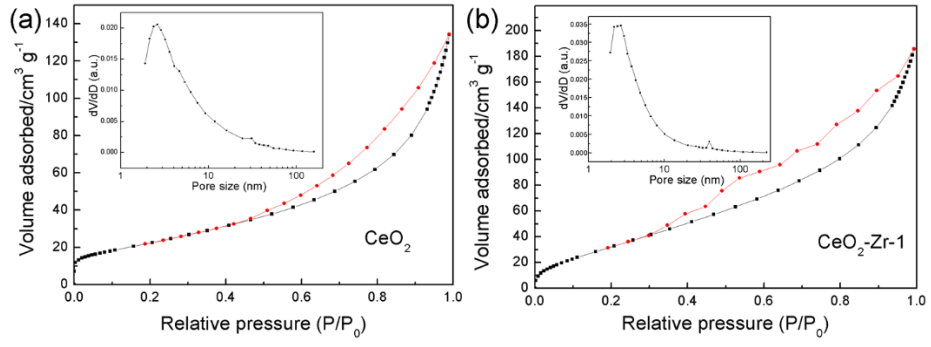


Fig. 3  $N_2$  adsorption isotherms and pore size distributions of (a) pristine  $CeO_2$  and (b)  $CeO_2$ -Zr-1.

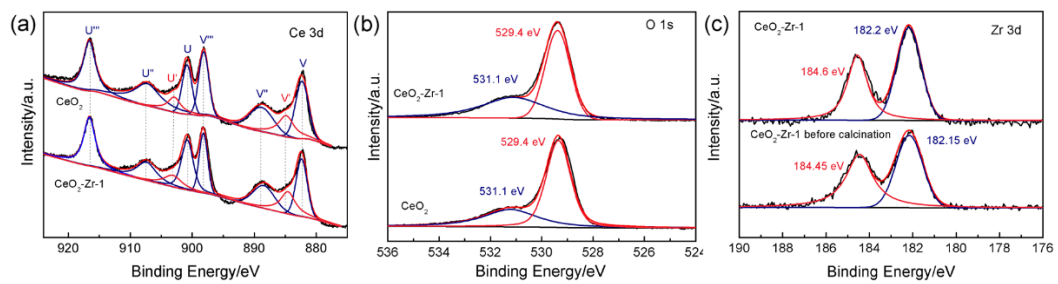


Fig. 4 (a) Ce 3d, (b) O 1s XPS spectra of pristine CeO<sub>2</sub> and CeO<sub>2</sub>-Zr-1, (c) Zr 3d

XPS spectrum of CeO<sub>2</sub>-Zr-1.

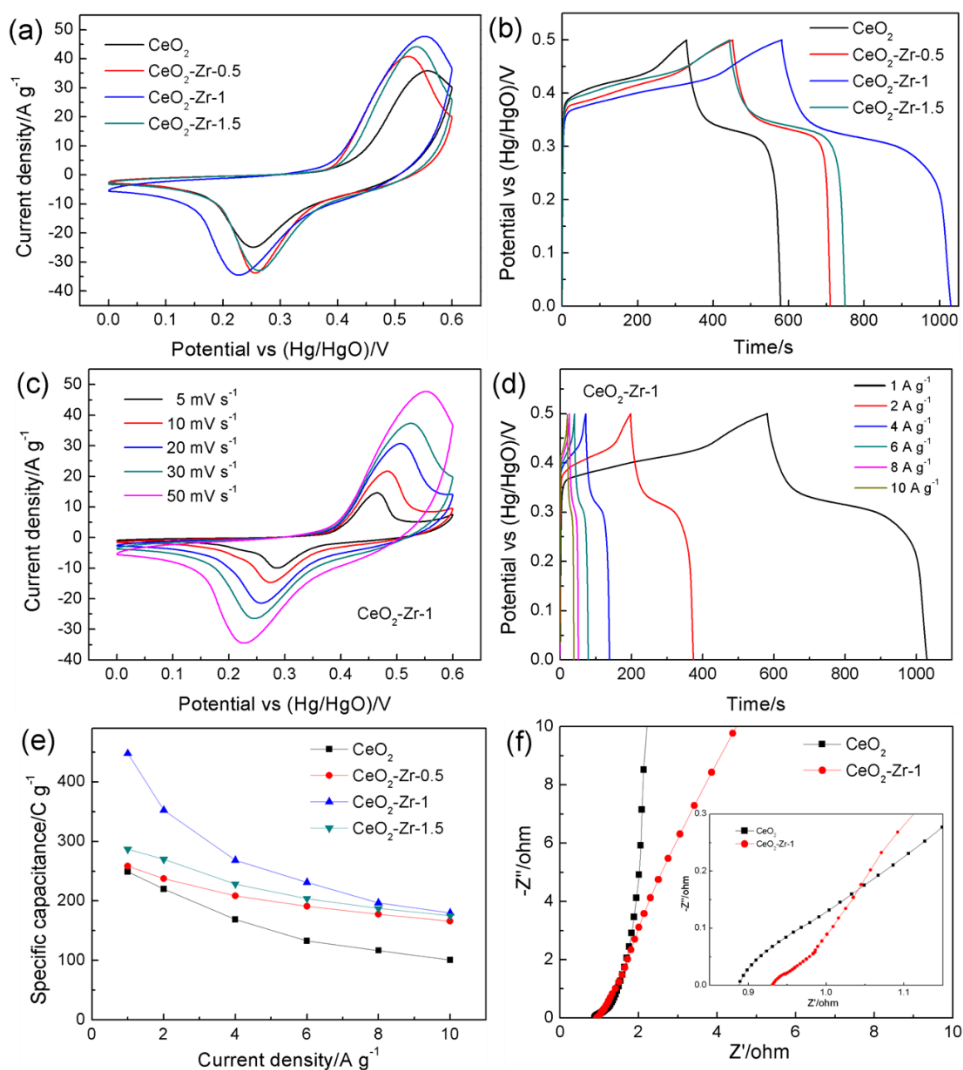


Fig. 5 (a) CV curves at a scan rate of  $50 \text{ mV s}^{-1}$  and (b) GCD curves at a current density of  $1 \text{ A g}^{-1}$  for the  $\text{CeO}_2$ ,  $\text{CeO}_2\text{-Zr-0.5}$ ,  $\text{CeO}_2\text{-Zr-1}$  and  $\text{CeO}_2\text{-Zr-1.5}$  electrodes, (c) CV curves measured at multiple scan rates and (d) GCD profiles at different current densities for the  $\text{CeO}_2\text{-Zr-1}$  electrodes, (e) specific capacities at various current densities of the  $\text{CeO}_2$ ,  $\text{CeO}_2\text{-Zr-0.5}$ ,  $\text{CeO}_2\text{-Zr-1}$  and  $\text{CeO}_2\text{-Zr-1.5}$  electrodes and (f) EIS Nyquist plots for the  $\text{CeO}_2$ , and  $\text{CeO}_2\text{-Zr-1}$  electrodes (the potential vs (Hg/HgO) is 0.5 V). (Inset: the magnified section at high frequency region).

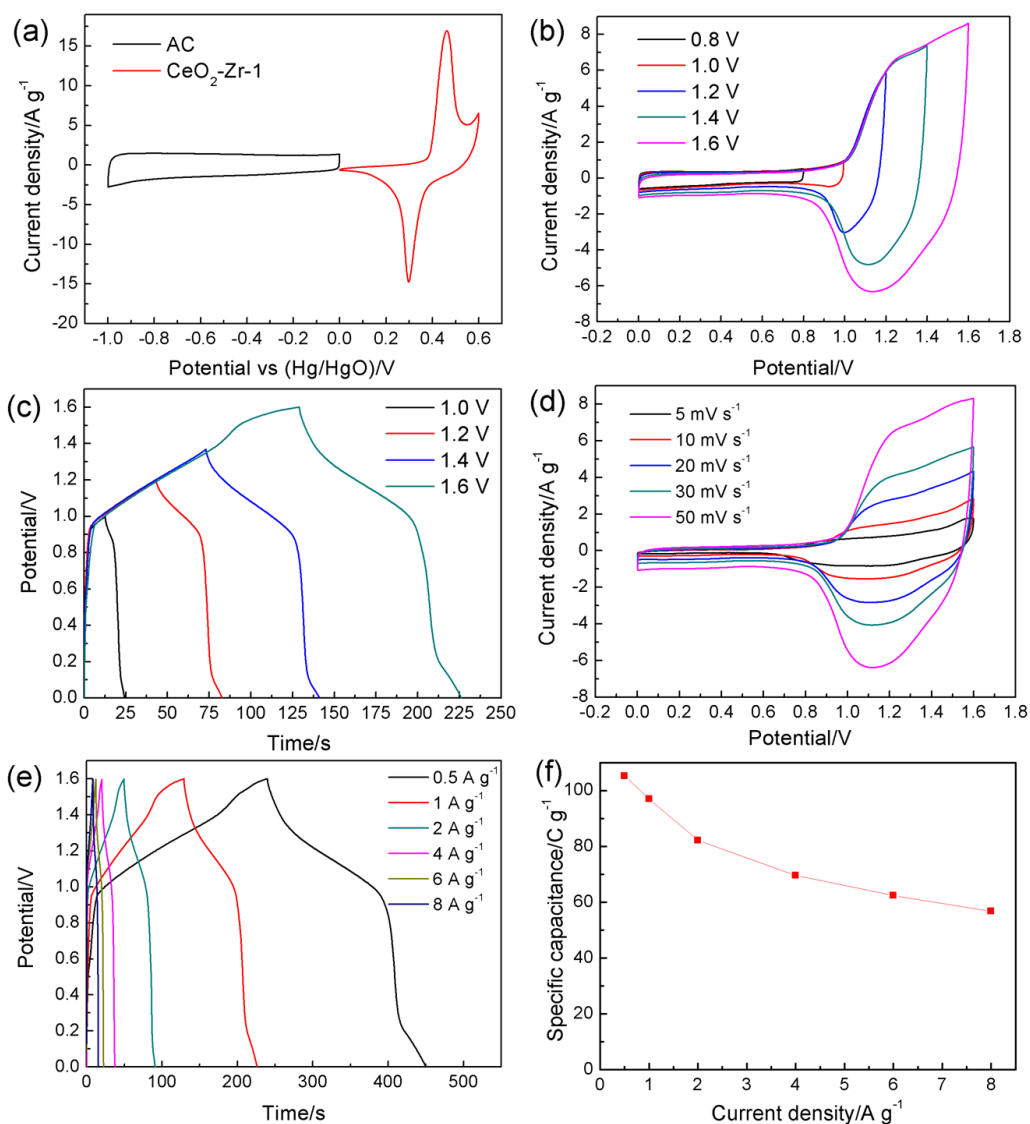


Fig. 6 (a) CV curves of AC and CeO<sub>2</sub>-Zr-1 electrodes measured in three electrode system at a scan rate of 10 mV s<sup>-1</sup>; (b) CV curves (scan rate: 50 mV s<sup>-1</sup>) and (c) GCD curves (current density: 1 A g<sup>-1</sup>) of the CeO<sub>2</sub>-Zr-1//AC ACS at different potential windows; (d) CV curves of the CeO<sub>2</sub>-Zr-1//AC ACS device at various scan rates, (e) GCD curves and (f) corresponding specific capacity of the CeO<sub>2</sub>-Zr-1//AC ACS at different current densities.

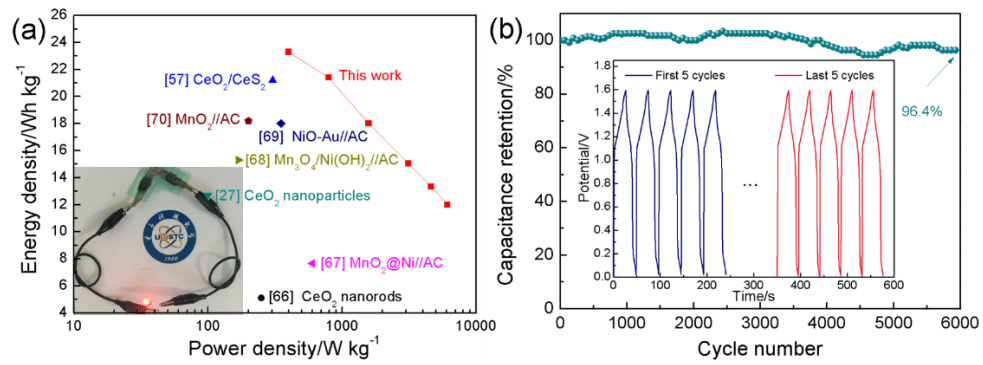


Fig. 7 (a) Ragone plot of the CeO<sub>2</sub>-Zr-1//AC ACS device (energy density vs power density) and comparison with those reported devices in the literature, (b) Cycling stability of the CeO<sub>2</sub>-Zr-1//AC ACS device at 6 A g<sup>-1</sup>.